國立清華大學

碩士論文

雷射誘發金屬線輻射

Laser-induced Metal-wire Radiation

系所別:光電工程研究所

學號姓名:9866506 陳子祥 (TzuHsiang Chen)

指導教授:黃衍介 博士 (Dr. Yen-Chieh Huang)

中華民國 一百年十一月

Abstract

Laser-Induced Plasma Radiation with gigahertz frequency could be used as an input energy source for a photocathode RF gun to replace the conventional input process. The resonant frequency of our target photocathode RF gun is 2.856GHz which means, a plasma radiation with a frequency of 2.856GHz has to be used in order to achieve the resonance condition.

Radiation frequency within the range of 2.3-2.6GHz had been successfully detected with a 1064 nm fundamental wave at pulse duration of 460 picoseconds, and a second harmonic wave (wavelength = 532mn) is generated from the fundamental wave with a LBO at a shorter pulse duration of 330 picoseconds. It is expected that, with a shorter pulse width, higher frequency radiation (hopefully can be near 2.856GHz) in the S-band region could be achieved.

Due to detection limitation of our ring-antenna, we cannot actually measure such a high frequency of plasma radiation created by a second harmonic wave. But if what we predicted is true, by replicating our current experiment with an enhanced ring-antenna, a kilowatt or even megawatt radiation power with an S-band frequency may be able to achieve and could possibly be recognized as a perfect substitution for the tradition powering method of a photocathode RF gun

Acknowledgement

寫了通篇英文的論文，雖然致謝也很想用英文來表達卻怎麼也沒法如中文般把諸多想法、感觸都融入字句。這兩年多來的時間，要用風雨飄搖來形容是有些太過了，不過一路上跌跌撞撞也終是熬出了頭，學到了許多為人處事，增長了不少見聞經驗，這一回顧，彷彿碩士班的同學們都才剛進到這個實驗室，大家雖不甚熟悉卻依然很快地打成一片，很開心這段時間跟你們一起有的共同回憶，一塊成長、學習以及探討。

謝謝昶志、佳穎、明耘及鈺中，除了實驗室相關的事情以外，在生活上也受到了你們許多的幫助；謝謝碩泰、寵棟學長，即使已在外面工作仍不時照顧在實驗室的學弟妹們；謝謝彥穎學長這一段日子以來研究上的指導以及生活方面的分享；謝謝永賢、安凱，在實驗上給了我許多的幫助讓我能順利進行實驗；謝謝老陳熱心幫忙，幫我製作了許多實驗元件，佔用了你不少周末，真的很感謝；謝謝 Shayeganrad 夫婦，從你們身上得到了不少照顧，也讓我學習到了有別於台灣的不同風情。特別感謝家祥及冠諺學長，在最後緊要關頭義氣相挺，給了我巨大的幫忙，讓我能順利完成學業；彥豪、芙涵、民雄、欣寧還有許許多多的人，大家都是我碩士生涯精彩的一部分。

謝謝我的指導教授黃衍介老師，除了研究上的傳道、授業，更是在我人生經驗的開導者，老師雖然嚴厲卻不乏人情，完全不遺餘力地照顧著我們研究群的每一個人，也請老師保重健康，勿過於勞幽。

謝謝我的家人們，血濃於水的親情不是幾段話可以描述的，是你們默默的在每一個地方無微不至的支持以及鼓勵，讓我能如此安心的在求學的環境中成長及茁壯，而我也終於能讓你們放下心中一塊大石頭，順利的畢業往下一個人生里程邁進，這次該換我來當你們的支持了。

最後要謝謝我的老婆，在這段如此需要我的日子裡，仍然給予了我最大的支持，心中滿懷著感動以及不少的歉意，未來我會更積極地向前，會給你最好的生活，一日夫妻百日恩，這輩子的緣分是百世修來的福份，謝謝妳。

僅以此文獻給我研究生涯中的每一個人，對你們我仍有著許多文字表達不出來的感謝，與你們共同度過的每一分回憶都是我日後珍惜的記憶，曾經經歷過的挫折、失敗，曾經綻開的快樂、歡笑，曾經流下的汗水、辛勞，這所有的一切讓我成為一個更好的人，謝謝你們。

Table of Contents

List of Tables

List of Figures

Chapter 1 Introduction

1.1 Motivation

Plasma acts as a source of electromagnetic radiation which comprises of a broad range of the spectrum including infrared, visible light, ultraviolet and X-rays radiation. Terahertz wave emission from laser-induced plasmas was first observed in 1993[1] and this terahertz generation had been further studied in plasma yielded from different states of matters including, air[2-3], liquid[4], semi-conductor[5] & conductor.

Among those plasma-induced radiation studies, researchers mainly put their focus on the detection of terahertz emissions as terahertz radiation plays an important role in many of daily life applications such as; spectroscopy[6], surveillance for security screening and for medical imaging[7]. Rationale for generating a lower frequency plasma radiation e.g. a gigahertz emission and its purpose had not been fully researched. As a reason of this, plasma radiation which lies along the S-band of the optical spectrum is worth for us to further explore.

A gigahertz radiation can served as an energy input for initiation of the electron acceleration in a photocathode RF gun given that, the emission frequency equals to the resonant frequency and with an accurate radiation phase. For the conventional energy input method, massive power supply and numerous devices had be used (e.g. a laser oscillator, a temporal pulse shaper, a pulse stretcher, an amplifier, a pulse compressor and a frequency converter) in order to generate an S-band radiation. In view of this, an easier, simpler and energy conservable method to obtain a comparable energy source i.e. the gigahertz radiation, will be of our great interest.

1.2 Laser-induced Wire Radiation

A directional electric current can be induced by frequency-mixing of matters in plasma condition, or by electron radiation via dipole antenna. Our current experiment used high power laser to breakdown the structure of copper wire, the energetic electrons would escape from the copper ion and inducing a return current.

As the return current evolves with time, the wire will behave like a current-carrying antenna and emits radiation.

Both copper plate and copper wire had been adopted as the target of our experiment at the initial stage. By considering their emission intensity, copper wire was found to have a higher emission rate than the copper plate and its current path was more directional as well. As the reason of this, copper wire had been chosen as our target material in the later experiments.

1.3 Overview

In Chapter 1, we had already presented our motivation that give rise to this paper. Further down the chapters, first of all in Chapter 2, a brief introduction and theory of all the techniques that we had applied in the experiment will be given. Moreover, experimental results and a brief discussion will be presented in Chapter 3 and last but not the least, our conclusion and possible future works will be mentioned in Chapter 4.

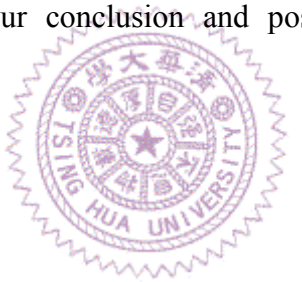

Chapter 2 Theory and Analysis

2.1 Nd:YAG Amplifier

In order for us to obtain a high energy laser for generating laser-induced plasma, a crystal composed of neodymium-doped yttrium aluminium garnet (Nd:YAG) is used as the laser gain medium with Xe flash lamp pumping to amplify the 1064nm fundamental wave. How efficient the Nd:YAG amplifier can perform mainly depends on the "small signal gain" of the gain medium. The small signal, single-pass gain can be defined as[8]:

$$G_0 = \exp(g_0 l) \tag{2.1.1}$$

where l is the length of gain medium and g_0 is the small signal gain coefficient given by:

$$g_0 = \sigma N \tag{2.1.2}$$

where σ is the stimulated emission cross section and N is the population inversion.

According to the rate equation for a four-level system, take Nd:YAG medium as an example, when we deriving N in the above equation 2.1.2, the energy level diagram is shown below:

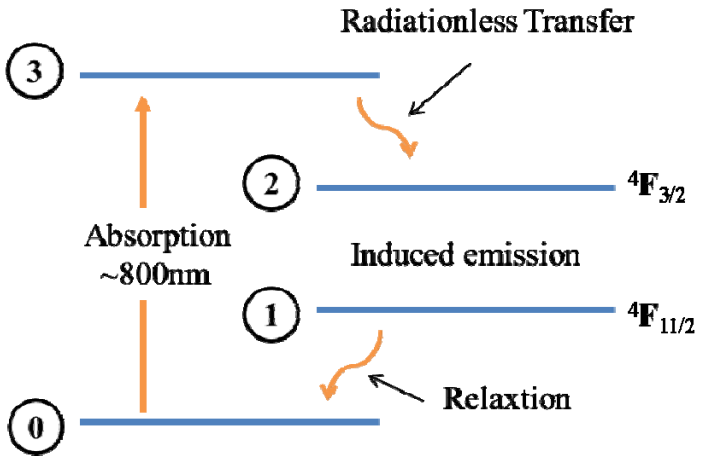

Fig. 2.1.1 Energy level diagram of Nd:YAG.

Once the energy pumped by the Xe flashlamp is absorbed by the Nd ions, they make a quick transition from ground state 0 to state 3 and then transfer to state 2

immediately. As a reason of this, we can assume N_3 is approximately 0, where N_i represents the number of atoms per unit volume occupying energy level *i*, and the rate equations can be written as follow:

$$\frac{dN_2}{dt} = W_p N_0 - (N_2 - N_1)\sigma\phi\, c - (\frac{N_2}{\tau_{21}} + \frac{N_2}{\tau_{20}}) \tag{2.1.3}$$

$$\frac{dN_1}{dt} = (N_2 - N_1)\sigma\phi\, c + \frac{N_2}{\tau_{21}} - \frac{N_1}{\tau_{10}} \tag{2.1.4}$$

Therefore, $$N_t = N_0 + N_1 + N_2 \tag{2.1.5}$$

where W_p is the pumping rate, σ is the stimulated emission cross section, ϕ is the photon density, c is the speed of light and τ_{ij} is the relaxation time from level *i* to level *j*.

In an ideal four levels system, τ_{10} is almost set to be 0, then it follows from (2.1.4) that, $\frac{dN_1}{dt} = 0$. We can rewrite equation (2.1.3) as

$$\frac{dN_2}{dt} = W_p N_0 - N_2\sigma\phi\, c - \frac{N_2}{\tau_f} \tag{2.1.6}$$

where $N = N_2 - N_1 = N_2$ is the inversion population density, and $N_t = N_0$ since $N_2 << N_0$. The fluorescence decay time τ_f of state 2 is given by

$$\frac{1}{\tau_f} = \frac{1}{\tau_{21}} + \frac{1}{\tau_{20}} \tag{2.1.7}$$

Given that, $\frac{dN_1}{dt} = 0$, we can assume the absence of amplifier radiation ($\phi = 0$) during the pumping scheme. N can simply be derived from equation (2.1.4) as

$$N = N_2 = N_0 W_p \tau_f \tag{2.1.8}$$

By applying equation (2.1.8) into equation (2.1.2), the gain coefficient can be re-written as

$$g_0 = \sigma N_0 W_p \tau_f \tag{2.1.9}$$

As there is always a loss of energy during the energy flow from Xe pumping to the laser output, therefore we should revise g_0 as

$$g_0 = \sigma(\frac{\eta_Q \eta_S \eta_B P_a}{h\nu_l V})\tau_f = \sigma[\frac{\eta_Q \eta_S \eta_B (\eta_P \eta_t \eta_a P_{in})}{h\nu_l V}]\tau_f \tag{2.1.10}$$

where ν_l is the transition frequency, h is the Plank's constant, V is the rod

volume, η_Q is the quantum efficiency, η_S is Stokes factor, η_B is the factor of beam overlapping, η_P is the pump efficiency of amplifier, η_t is the transfer efficiency, η_a is the absorption efficiency, P_{in} is the input power from Xe flashlamp pumping and P_a is absorbed pump power.

By combining equation (2.1.1) and equation (2.1.10), we have

$$G_0 = \exp(g_0 l) = \exp(\frac{\sigma \tau_f \eta_Q \eta_S \eta_B \eta_P \eta_t \eta_a P_{in}}{h\nu_L V} l) \tag{2.1.11}$$

The probability of an absorbed pump photon producing an active atom in state 3 is determined by the quantum efficiency η_Q, expressed as:

$$\eta_Q = \left(\frac{\gamma_{32}}{\gamma_{32} + \gamma_{31} + \gamma_{30}} \right) = \left(1 + \frac{\tau_{32}}{\tau_{31}} + \frac{\tau_{32}}{\tau_{30}} \right)^{-1} \tag{2.1.12}$$

The Stokes factor η_S represents the ratio between the radiated photon energy $h\nu_L$ and the absorbed pumping photon energy $h\nu_P$,

$$\eta_S = \frac{h\nu_L}{h\nu_P} = \frac{\lambda_P}{\lambda_L} \tag{2.1.13}$$

where λ_P is the pumping wavelength and λ_L is the wavelength of laser. The beam overlapping efficiency η_B measures the spatial overlap between the input beam and the gain distribution in the laser gain medium, defined as

$$\eta_B = \frac{\pi w_m^2}{\pi w_P^2} \tag{2.1.14}$$

where w_m is the beam radius of laser and w_P is the beam radius of pumping. The pump efficiency of amplifier η_P is defined as the ratio of stored energy to pump energy,

$$\eta_P = \frac{P_\lambda}{P_{in}} = \int_{\lambda_1}^{\lambda_2} \frac{P_\lambda' d\lambda}{P_{in}} \tag{2.1.15}$$

where P_λ is the spectral output power of the flashlamp within the absorption bands of the gain medium. The transfer efficiency η_t represents the efficiency of flashlamp pump radiation to the laser medium during energy transfer (for close coupled cavities, the typical values are 0.3–0.6). The absorption efficiency η_a is the ratio of absorbed power by the laser medium to the power entering the laser medium,

$$\eta_a = 2\alpha_0 R \cdot \exp(-\alpha_0 R) \tag{2.1.16}$$

where α_0 is the absorption coefficient of Nd:YAG averaged over the spectral emission range of the flashlamp and R is the Nd:YAG rod radius.

However, the growth of input energy is said to be exponential only when the energy input is in low power. If we consider a general case, the energy gain for a light passing through a laser amplifier is given by

$$G = \frac{E_s}{E_{in}} \ln\left\{1 + \left[\exp(\frac{E_{in}}{E_s}) - 1\right] G_0\right\} \tag{2.1.17}$$

where E_s is saturation fluence which can be defined by

$$E_s = \frac{J_{st}}{\gamma g_0} \tag{2.1.18}$$

where γ=1 for 4-level system and $J_{st} = g_0 E_s$ is the store energy per volume. E_{in} is the input energy per unit area and g_0 is the small signal gain coefficient. When the energy input is in low power, E_{in}/E_s is much smaller than 1, the energy gain is approximately the same as small signal gain G_0 and is exponential with amplifier length. For a high-level energy input, where E_{in}/E_s is much larger than 1, G will turn out to be approximately $1+(E_s/E_{in})g_0 l$, thus, the energy is linear with the length of the gain medium.

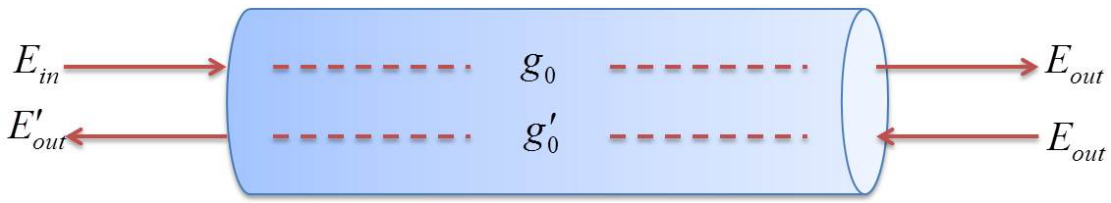

Fig. 2.1.2 Schematic of single- and double-passes amplifier.

By now, the equation (2.1.17) can be rearranged in terms of the input and output energy. With the notation in Fig. 2.1.2, the output energy fluence of single-pass amplifier is given by

$$E_{out} = E_s \ln\left\{1 + \left[\exp(\frac{E_{in}}{E_s}) - 1\right] \exp(g_0 l)\right\} \tag{2.1.19}$$

The output fluence E'_{out} of double-pass amplifier can be calculated from equation (2.1.19) as follows:

$$E'_{out} = E_s \ln\left\{1 + \left[\exp(\frac{E_{iout}}{E_s}) - 1\right]\exp(g'_0 l)\right\} \quad (2.1.20)$$

the return gain coefficient g'_0 is shown below

$$g'_0 = (1 - \eta_E) g_0 \quad (2.1.20)$$

and

$$\eta_E = (E_{out} - E_{in}) / g_0 l E_s \quad (2.1.21)$$

where η_E is the extraction efficiency.

2.2 Second Harmonic Generation (SHG)

Second harmonic generation (SHG) is a well-known technology that generates the frequency-doubled signal in a nonlinear medium (usually in a bulk crystal). The lack of symmetry at the surface (or a buried interface) can lead to the generation of light at a frequency twice that of the incident light. In practical, when a single pump wave at the frequency ω is emitted into a nonlinear medium, a second harmonic wave with a frequency of 2ω can be generated simultaneously.

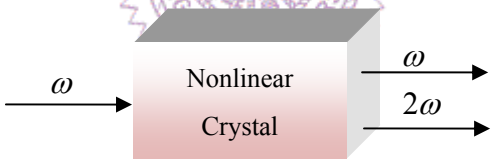

Fig. 2.2.1 Simple schematic for the second harmonic generation (SHG) process.

This light propagation phenomenon in a nonlinear medium can be defined in wave equations and the optical response of a medium is expressed in terms of the induced nonlinear polarization $\vec{P}_{NL}$ [9].

According to Maxwell's equations:

$$\nabla \times \vec{E} = -\frac{\partial \vec{B}}{\partial t} \quad (2.2.1)$$

$$\nabla \times \vec{H} = \frac{\partial \vec{D}}{\partial t} \quad (2.2.2)$$

$$\vec{D} = \varepsilon_0 \tilde{\varepsilon}_r \vec{E} + \vec{P}_{NL} \quad (2.2.3)$$

where $\vec{E}$ is the electric field, $\vec{B}$ is the magnetic flux density, $\vec{D}$ is the electric flux density, ε_0 is the vacuum permittivity, ε_r is the relative permittivity and μ_0 is the permeability. When reconstructing the above equations, the input electric filed can be found as:

$$\nabla^2 \vec{E} - \frac{\overset{\approx}{\varepsilon}_r}{c_0^{\,2}} \frac{\partial^2 \vec{E}}{\partial t^2} = \mu_0 \frac{\partial^2 \vec{P}_{NL}}{\partial t^2} \tag{2.2.4}$$

If we consider the incoming field as the plane wave, the field will be proportional to exp(jωt-kz), where k is the wave vector at frequency ω. By assuming the wave propagates along z direction, we can have electric field as:

$$\tilde{\vec{E}}(z,t) = \frac{1}{2}\left[\tilde{\vec{E}}(z,\omega)e^{j(\omega t - \vec{k}\cdot\vec{z})} + c.c.\right] = \frac{1}{2}\left[\vec{\tilde{E}}(z,\omega)e^{j(\omega t)} + c.c\right] \tag{2.2.5}$$

And $$\tilde{\vec{P}}_{NL}(z,t) = \frac{1}{2}\left[\tilde{\vec{P}}_{NL}(z,\omega)e^{j(\omega t - \vec{k}\cdot\vec{z})} + c.c\right] = \frac{1}{2}\left[\vec{\tilde{P}}_{NL}(z,\omega)e^{j(\omega t)} + c.c.\right] \tag{2.2.6}$$

If we engage equation (2.2.5) and (2.2.6) with (2.2.4), the initial term can be re-written as

$$\nabla^2 \tilde{\vec{E}} = [\frac{1}{2}\frac{\partial^2 \tilde{\tilde{E}}}{\partial z^2} - jk\frac{\partial \tilde{\tilde{E}}}{\partial z} - \frac{1}{2}k^2 \tilde{\tilde{E}}]e^{j(\omega t - \vec{k}\cdot\vec{z})} + c.c. \tag{2.2.7}$$

As the propagating plane wave is paraxial, we can apply the slowly varying envelope approximation condition (SEVA) given that the amplitude of the wave changes very slowly within a distance of its wavelength. And here we get

$$\left|\frac{\partial^2 \tilde{\tilde{E}}}{\partial z^2}\right| << \left|k\frac{\partial \tilde{\tilde{E}}}{\partial z}\right| \tag{2.2.8}$$

Under this condition, we can simplify equation (2.2.7) as

$$\nabla^2 \tilde{\vec{E}} = \frac{\partial \tilde{\vec{E}}}{\partial z^2} \approx [-jk\frac{\partial \tilde{\tilde{E}}}{\partial z} - \frac{1}{2}k^2 \tilde{\tilde{E}}]e^{j(\omega t - \vec{k}\cdot\vec{z})} + -\frac{1}{2}k^2 \tilde{\tilde{E}}e^{j(\omega t - \vec{k}\cdot\vec{z})} + c.c. \tag{2.2.9}$$

and finally, we will get

$$\frac{\partial \tilde{\tilde{E}}(z,\omega)}{\partial z} = -j\frac{\mu_0 c_0 \omega}{2n_\omega}\vec{\tilde{P}}_{NL}(z,\omega)e^{j\vec{k}\cdot\vec{z}} \tag{2.2.10}$$

The nonlinear polarization can be presented by using Einstein summation convention as

$$\hat{P}_{NL,i}(z,\omega) = c^{(2)}\varepsilon_0 \sum_{j,k} \chi_{ijk}(-\omega,\omega_1,\omega_2)\ \hat{E}_j(z,\omega_1)\hat{E}_k(z,\omega_2) \qquad (2.2.11)$$

, where $\omega = \omega_1 + \omega_2$ and $c^{(2)}=1$ at $\omega_1 \neq \omega_2$ or $c^{(2)}=0.5$ at $\omega_1 = \omega_2$.

Combining equation (2.2.10) and (2.2.11) will result in

$$\frac{d\overline{E}_{2\omega}}{dz} = -j\kappa_{2\omega}\overline{E}_{\omega}^{2} e^{j\Delta\vec{k}\cdot\vec{z}} \qquad (2.2.12)$$

$$\frac{d\overline{E}_{\omega}}{dz} = -j\kappa_{\omega}\overline{E}_{2\omega}\overline{E}_{\omega}^{*} e^{-j\Delta\vec{k}\cdot\vec{z}} \qquad (2.2.13)$$

where $\Delta\vec{k} = 2\vec{k}_{\omega} - \vec{k}_{2\omega}$ represents the phase velocity mismatch and $\kappa_{\omega} = \frac{d_{eff}\omega}{c_0 n_{\omega}}$ is the coupling coefficient with the assumption of $n \approx n_{2\omega} \approx n_{\omega}$.

By assuming the pump power depletion is negligible, the pump power will remains its constant within the boundary distance, and thus $\frac{d\overline{E}_{\omega}}{dz} = 0$. Hence, the solution of the combining equation (2.2.12) and (2.2.13) will only depend on the former one, given by

$$\overline{E}_{2\omega}(z) = -jk\overline{E}_{\omega}^{2}(0)\cdot z \cdot e^{j\Delta kz/2}\sin c(\Delta kz/2) \qquad (2.2.14)$$

This equation can also be expressed in terms of the laser intensity by $I = \left|\overline{E}\right|^2 / 2Z$, where $Z = Z_0 / n_{\omega}$.

$$I_{2\omega}(z) = \frac{2Z_0 n_{2\omega}}{n_{\omega}^{2}}\kappa^2 I_{\omega}^{2}(0) z^2 \sin c^2(\Delta kz/2)$$

$$\approx 2Z\kappa^2 I^2{}_{\omega}(0) z^2 \sin c^2(\Delta kz/2) \qquad (2.2.15)$$

Therefore the intensity conversion efficiency will be

$$\eta_{2\omega} \equiv \frac{I_{2\omega}(z)}{I_0(0)} = \kappa^2 z^2 \left|\overline{E}_{\omega}(0)\right|^2 \sin c^2(\Delta kz/2)$$

$$\approx 2Z\kappa^2 I_{\omega}(0) z^2 \sin c^2(\Delta kz/2) = \Gamma^2 z^2 \sin c^2(\Delta kz/2) \qquad (2.2.16)$$

where $\Gamma^2 \equiv \kappa^2 \left|\overline{E}_{\omega}(0)\right|^2$.

The phase mismatching effect is show in Fig.2.2.2 and it is obviously showing in the graph that the maximum conversion efficiency occurs at $\Delta k = 0$ where the phase-matching condition appears at that point.

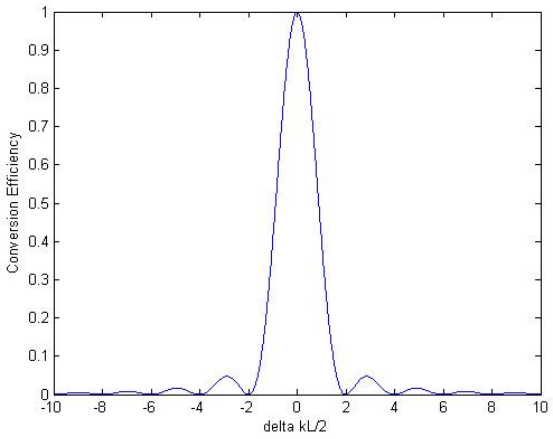

Fig. 2.2.2 Schematic for the sinc^2 function of the conversion efficiency.

However, since materials are dispersive in nature, the refractive index will be a function of emission wavelength, and thus, for SHG process in free space, the matching condition cannot be fulfilled. But this phase matching condition will exist in some special cases such as in a birefringent media.

There are two optic axes lie in the XZ plane in a biaxial crystal. Consider a case of laser propagation at angle θ and ϕ which respect to the Z-axis and X-axis, as illustrated in Fig.2.2.3, the angle Ω for the optic axis is defined with respect to the Z-axis. The general refractive indices can be written as

$$\frac{\sin^2\theta\cos^2\phi}{n^{-2}-(n_x)^{-2}}+\frac{\sin^2\theta\sin^2\phi}{n^{-2}-(n_y)^{-2}}+\frac{\cos^2\theta}{n^{-2}-(n_z)^{-2}}=0 \qquad (2.2.17)$$

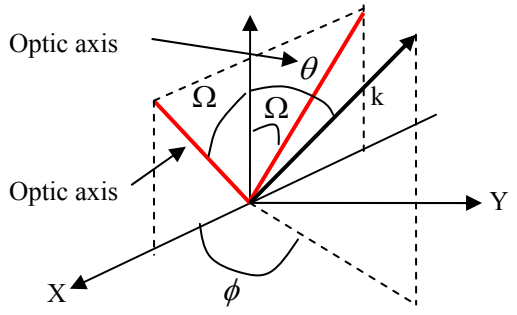

Fig. 2.2.3 A wave propagates along k direction with angles θ and ϕ.

Lithium triborate or LiB3O5 (LBO) which is adopted in our current experiment is used here as an example. LBO is a negative biaxial crystal with a large effective SHG coefficient which is 3 times larger than the one of KDP crystal, so it is widely

used to be the medium of SHG process. The other properties of LBO are listed below:

Table 2.2.1 LBO Properties.

Chemical Formula	**LiB_3O_5**
Sellmeier Equations	$n_x^2 = 2.4542 + 0.0113 / (\lambda^2 - 0.0114) - 0.0139\lambda^2$
	$n_y^2 = 2.5390 + 0.0128 / (\lambda^2 - 0.0119) - 0.0185\lambda^2$
	$n_z^2 = 2.5865 + 0.0131 / (\lambda^2 - 0.0122) - 0.0186\lambda^2$
PM range (Type-I SHG)	554-2600nm
Nonlinearity d_{ij}	d_{31} = 1.09 pm/V
	d_{32} = 1.17 pm/V
d_{eff} for NCPM type-I SHG	$d_{eff} = d_{32}\cos\phi$
Damage Threshold	>10GW/cm^2 at 10ns for TEM_{00} 1064nm

For a NCPM LBO, it is featured by large angle acceptance, maximum effective coefficient and no walk off effect. Its theta and phi are designed at 90 and 0 degrees, respectively, as illustrated in Fig.2.2.4.

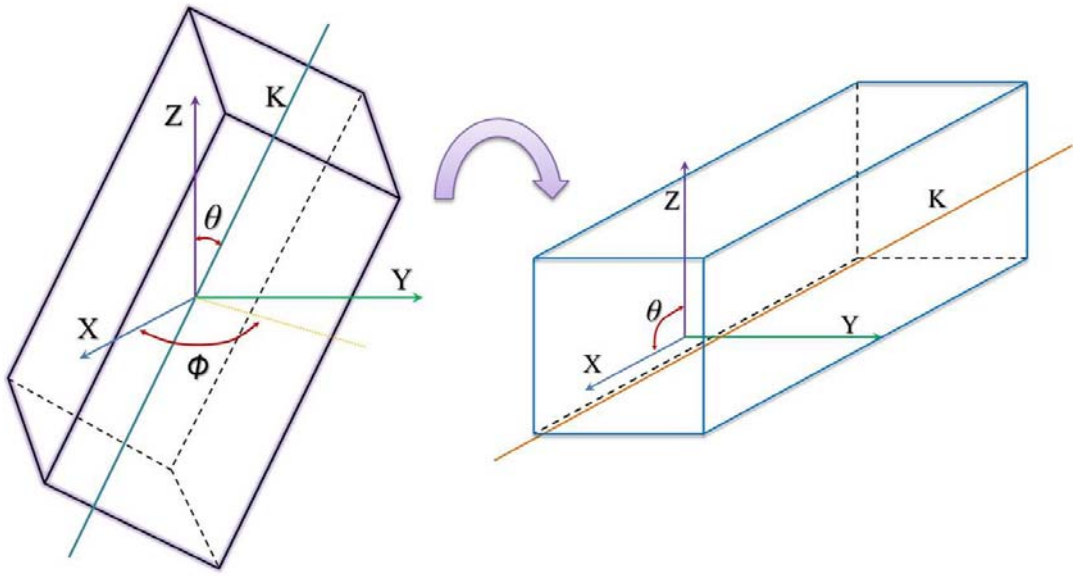

Fig. 2.2.4 Schematic of type-I NCPM LBO with θ=90 degrees and ϕ=0 degrees.

In other words, the incident wave will propagate along the X-axis of a LBO crystal, and we can have $n_o = n_y$ and $n_e = n_z$. For type I (ooe) phase matching condition, $\Delta k = 2\dfrac{2\pi n_{\lambda,o}}{\lambda} - \dfrac{2\pi n_{\lambda/2,e}}{\lambda/2}$ achieves to be 0 by operating temperature T at T_{pm}.

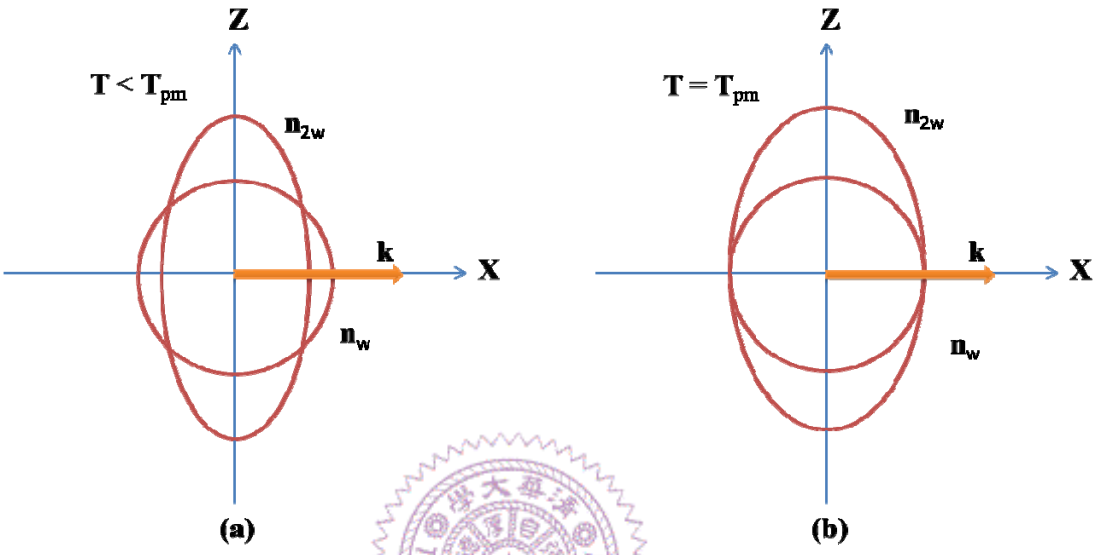

Fig. 2.2.5 The refractive index surface of biaxial crystals at XZ plane. (a) for $T<T_{pm}$ and (b) for $T=T_{pm}$.

The temperature dependence is shown in Fig. 2.2.6 where the theoretical phase matching temperature is at 148°c.

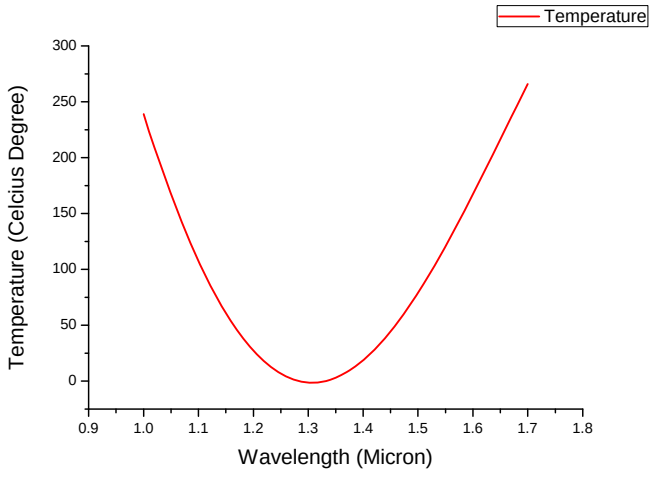

Fig. 2.2.6 Temperature dependence for NCPM LBO.

2.3 Laser-induced Wire Radiation

When an intense laser, which has one end grounded as shown in Fig. 2.3.1, with ultra-short pulse impacts on a thin wire target, electrons will be kicked out and cause a return current through the wire[10]. This behavior acts like a current-carrying antenna that can generate electromagnetic radiations at which the frequency relates to the laser pulse width.

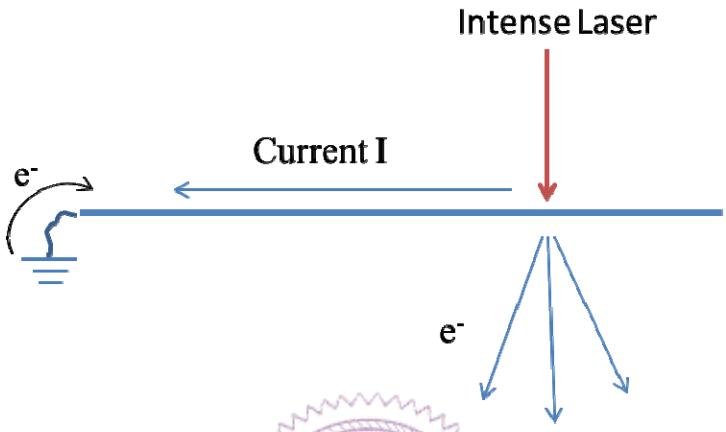

Fig. 2.3.1 The return current modle.

The leading edge of the laser pulse rapidly heats, melts and vaporizes the surface of the wire. The vaporization and initial ionization of atoms is shown below:

$$M_{(s)} + h\nu \rightarrow M^{+}{}_{(g)} + e^{-}$$

Although most of the excited electrons are draw back to the wire due to the strong electric field induced by the charges separation, there are still some electrons with higher energies that can escape from the wire.

To analyze the radiation of a straight conducting wire (linear antenna), we consider an elemental oscillating dipoles in free space, as shown in Fig. 2.3.2. Assume the current in the wire is uniform and sinusoidally vary with time[11]:

$$i(t) = I\cos\omega t = \mathrm{Re}\left[Ie^{j\omega t}\right] \qquad (2.3.1)$$

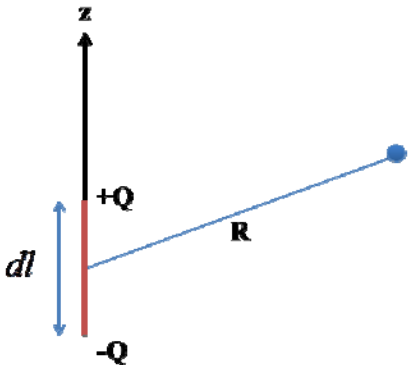

Fig. 2.3.2 The elemental electric dipole.

The vector potential $\vec{A}$ can be derived from the current distribution in the wire with phase constant $\beta = k_0 = 2\pi/\lambda$ and radius R.

$$\vec{A} = a_z \frac{\mu_0 I d\ell}{4\pi}\left(\frac{e^{-j\beta R}}{R}\right) \tag{2.3.2}$$

Since $a_z = a_R \cos\theta - a_\theta \sin\theta$, the spherical components of $\vec{A} = a_R A_R + a_\theta A_\theta + a_\phi A_\phi$ are:

$$A_R = \frac{\mu_0 I d\ell}{4\pi}\frac{e^{-j\beta R}}{R}\cos\theta \tag{2.3.3}$$

$$A_\theta = -\frac{\mu_0 I d\ell}{4\pi}\frac{e^{-j\beta R}}{R}\sin\theta \tag{2.3.4}$$

$$A_z = 0 \tag{2.3.5}$$

Assume the magnetic field has no variation along coordinate ϕ. The magnetic field can be written as

$$\vec{H} = \frac{1}{\mu_0}\nabla \times \vec{A}$$

$$= -a_\phi \frac{I d\ell}{4\pi}\beta^2 \sin\theta\left[\frac{1}{j\beta R} + \frac{1}{(j\beta R)^2}\right]e^{-j\beta R} \tag{2.3.6}$$

The electric field can be obtained equation (3.4.6) by

$$\vec{E} = \frac{1}{j\omega\varepsilon_0}\nabla \times \vec{H} = \frac{1}{j\omega\varepsilon_0}\left[a_R \frac{1}{R\sin\theta}\frac{\partial}{\partial\theta}(H_\phi \sin\theta) - a_\theta \frac{1}{R}\frac{\partial}{\partial R}(RH_\phi)\right] \tag{2.3.7}$$

which gives

$$E_R = -\frac{I d\ell}{4\pi}\eta_0\beta^2 2\cos\theta\left[\frac{1}{(j\beta R)^2} + \frac{1}{(j\beta R)^3}\right]e^{-j\beta R} \tag{2.3.8}$$

$$E_R = -\frac{Id\ell}{4\pi}\eta_0\beta^2 \sin\theta\left[\frac{1}{j\beta R}+\frac{1}{(j\beta R)^2}+\frac{1}{(j\beta R)^3}\right]e^{-j\beta R} \tag{2.3.9}$$

$$E_\phi = 0 \tag{2.3.10}$$

where $\eta_0 = \sqrt{\frac{\mu_0}{\varepsilon_0}} = 120\pi = 377(\Omega)$.

When an observer is very closed to the dipole antenna in the region of near zone, $\beta R << 1 \Rightarrow R << \lambda/2\pi$. The leading term in equation (3.4.6) is $\frac{1}{(j\beta R)^2}$, so the simplified form becomes

$$H_\phi = \frac{Id\ell}{4\pi R^2}\sin\theta \tag{2.3.10}$$

Similarly, we can have simplified forms for electric fields as

$$E_R = -\frac{Id\ell}{4\pi}\eta_0\beta^2 2\cos\theta \tag{2.3.11}$$

$$E_R = -\frac{Id\ell}{4\pi}\eta_0\beta^2 \sin\theta \tag{2.3.12}$$

For far zone region, $\beta R >> 1 \Rightarrow R >> \lambda/2\pi$, equation (3.4.6) and (3.4.7) are reduced into the forms of

$$H_\phi = j\frac{Id\ell}{4\pi}\beta\sin\theta\frac{e^{-j\beta R}}{R} \tag{2.3.13}$$

$$E_\theta = j\frac{Id\ell}{4\pi}\frac{e^{-j\beta R}}{R}\eta_0\beta\sin\theta \tag{2.3.14}$$

The total input power P_i equals to P_r+P_l, where P_r is the radiation power and P_l is the power from ohmic loss in antenna itself. If we assume no ohmic losses , the radiated power in the far zone can be calculated as

$$P_r = \oint_s (\vec{E}\times\vec{H})\cdot S = \int_0^{2\pi}\int_0^{\pi}\frac{\eta}{32\pi^2}\frac{I^2 d\ell^2}{R^2}\beta^2\sin^2\theta R^2\sin\theta d\theta d\phi$$

$$= 2\pi\int_0^{\pi}\int_0^{2\pi}\int_0^{\pi}\frac{\eta}{32\pi^2}I^2 d\ell^2\beta^2\sin^3\theta d\theta$$

$$= \frac{\eta}{12}\frac{I^2 d\ell^2}{\pi}\beta^2 \tag{2.3.15}$$

Chapter 3 Experimental Result and Discussion

3.1 Experiment Setup

In order to enhance the output energy of the fundamental wave at 1064 nm that can breakdown the metal wire, an amplifier stage of Nd: YAG rod was adopted in this experiment. A double-pass configure is a good way to extract energy more efficiently and the result will be shown in section 3.2.

In section 3.3, we will describe the result of second harmonic generation, the shorter pulse width of SH wave will provide another laser source to process the further experiment.

In the last section, we will show the result that the S-band radiation can be produced by a thin wire antenna.

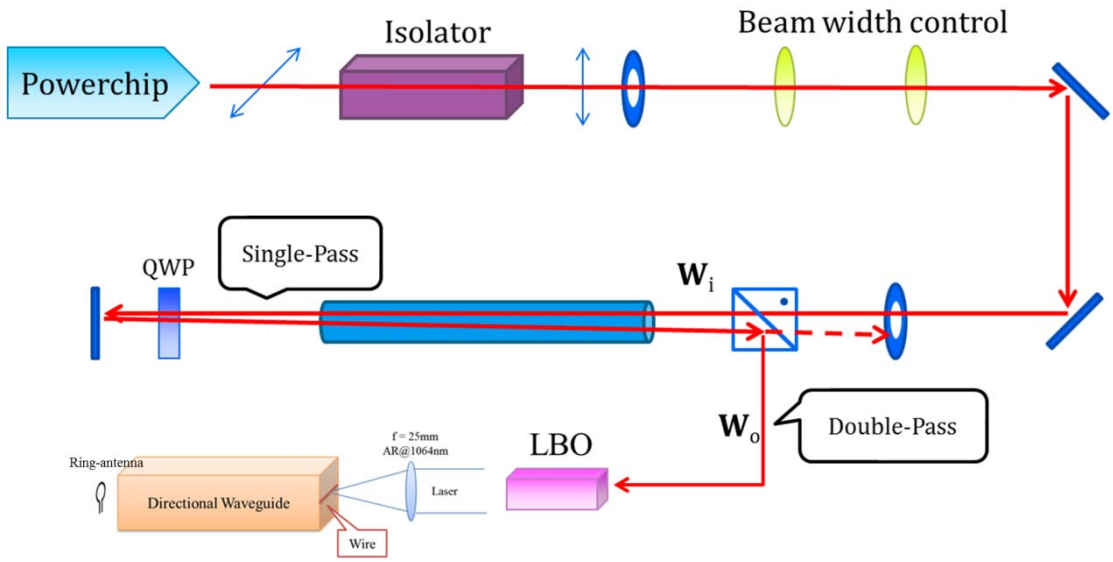

Fig. 3.1.1 The whole setup for Laser-induced Wire Radiation..

3.2 Flash lamp Pumped Nd:YAG Amplifier

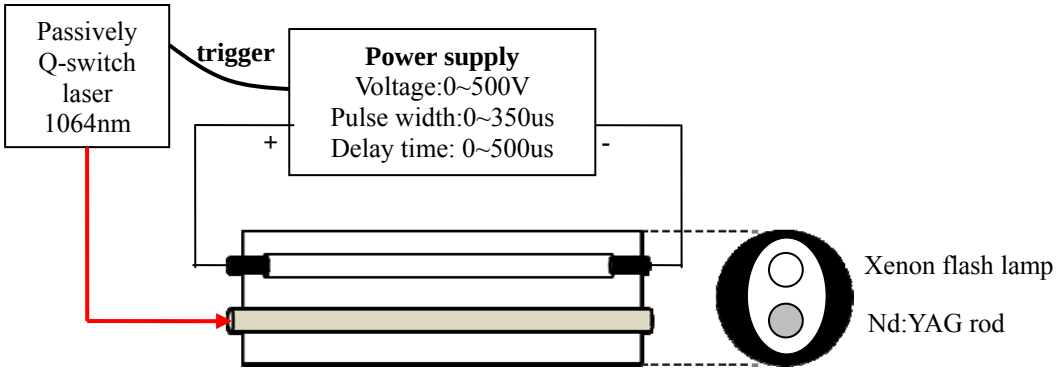

Fig. 3.2.1 Schematic of xenon flashlamp pumped Nd:YAG amplifier. The Nd:YAG rod of 4x120 mm^2 is installed inside the chamber.

In order to achieve a high energy fundamental wave, we used the Nd:YAG amplifier which is pumped by a xenon flashlamp. The wavelength of the fundamental wave is at 1064nm with 50 μJ pulse energy, 10Hz repetition rate and 460 ps pulse duration. In our previous experiments, we obtained 4 mJ output energy from a single pass amplifier with the gain of 110. However, if we want to get efficient energy extraction, the input-fluence should be comparable to the saturation-fluence of the laser transition. As a reason of this, a double-pass configuration will be a good way to obtain a higher gain.

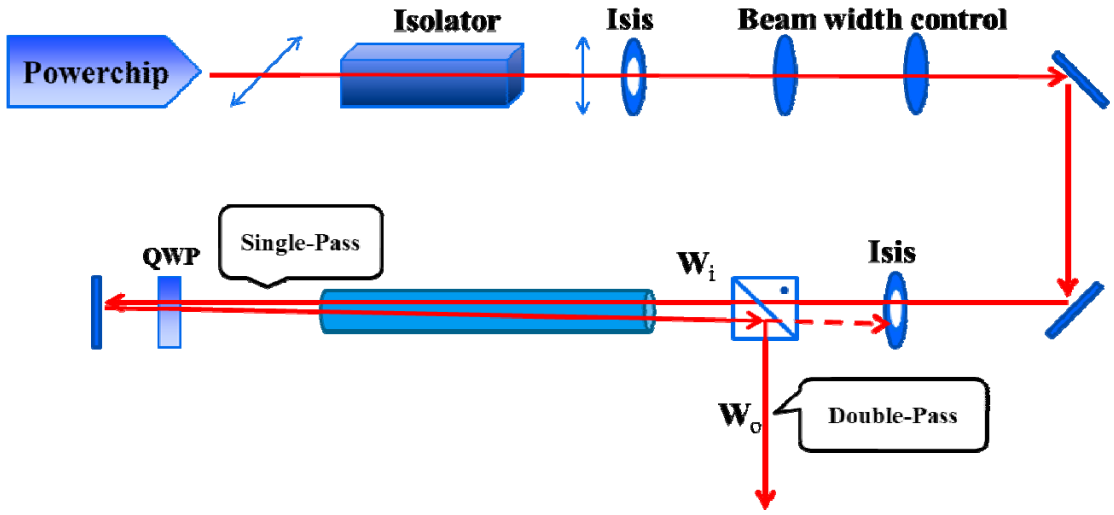

Fig. 3.2.2 Experiment setup for the double-pass amplifier.

In the double-pass amplifier system, the input beam and the reflected beam propagate along different paths to avoid the reflected beam return to the source laser via its original pathway. Hence, magnitude of the beam should be precisely controlled, the input beam radius W_i and the output beam radius W_o were accurately adjusted by the double-lenses system shown in Fig.. 3.2.2. The delay time of power supply was set to be 264 μs and the pulse width of xenon flashlamp was 350 μs . Relations of input voltage versus output energy with different beam width were shown below:

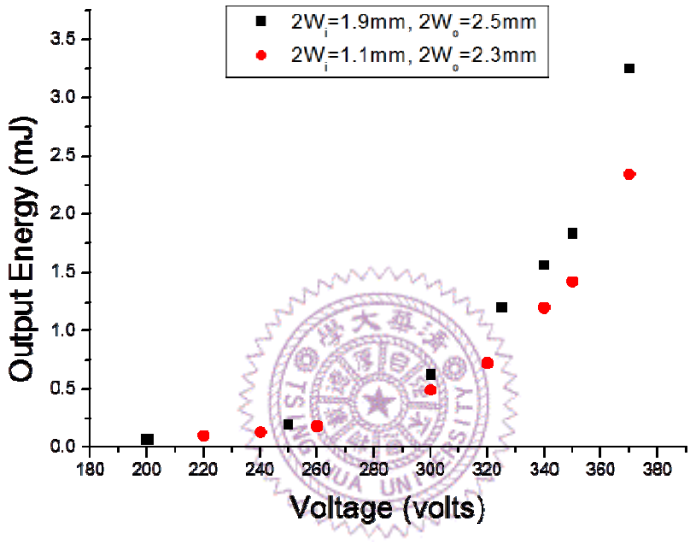

Fig. 3.2.3 The amplified output energy at 1064nm from the single-pass Nd:YAG amplifier.

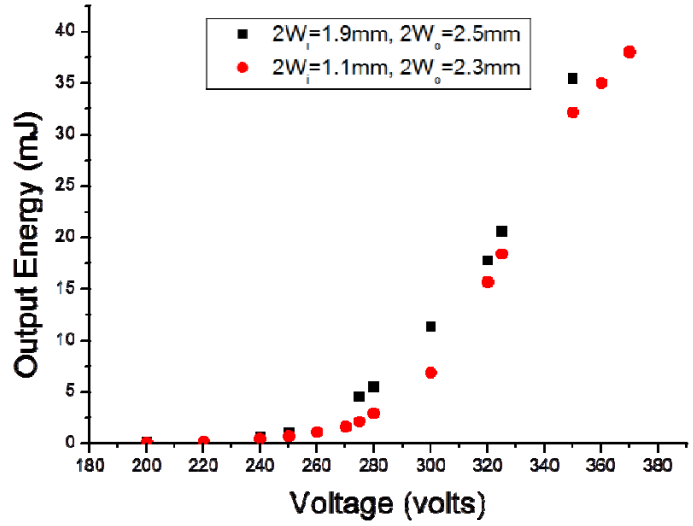

Fig. 3.2.4 The amplified output energy at 1064nm from the double-pass Nd:YAG amplifier.

According to the result with a single-pass amplifier in Fig. 3.2.3, the output energy was shown to be higher under the condition of a larger input beam spot size when compared to the smaller one. With an input voltage of 360 volts, the maximum output energy was 3.25 mJ when the input beam diameter was 2.5 mm whereas the maximum output energy was 2.3 mJ when the input beam diameter was 1.1mm. From equation (2.1.14), it is obvious that the better overlapping between the input beam and the gain distribution, the higher beam overlapping efficiency η_B we can obtain. The similar result was also shown in Fig. 3.2.4 with the double-pass amplifier; the maximum output energy was about 40 mJ with the reflected beam diameter of 2.5mm. Although the power supply used here can reach a maximum of 500v, an amplified spontaneous emission (ASE) occurred at applied voltage higher than 380 volts and this limited the maximum output energy to only ~380v.

Based on the above outcomes, a beam with $2W_i$ at 2.3 mm and $2W_o$ at 2.7 mm was applied in our experiment in order to optimize the output energy. Results are shown in Fig. 3.2.5 with a theoretical curve and error bar due to the energy instability from xenon flashlamp pumping. The parameters we used were calculated in Table 3.2.1[7].

Table 3.2.2 The simulation parameters used in Fig. 3.2.5

quantum efficiency η_Q	0.95
Stokes factor η_s	0.76
Beam overlap efficiency η_B	0.46
Pump source efficiency η_p	0.058
Transfer efficiency η_t	0.3
Absorption efficiency η_a	0.74
Stimulated emission cross section σ	$2.8\times10^{19}\text{cm}^2$
Length l of Nd:YAG rod	12cm
V	1.51cm^3

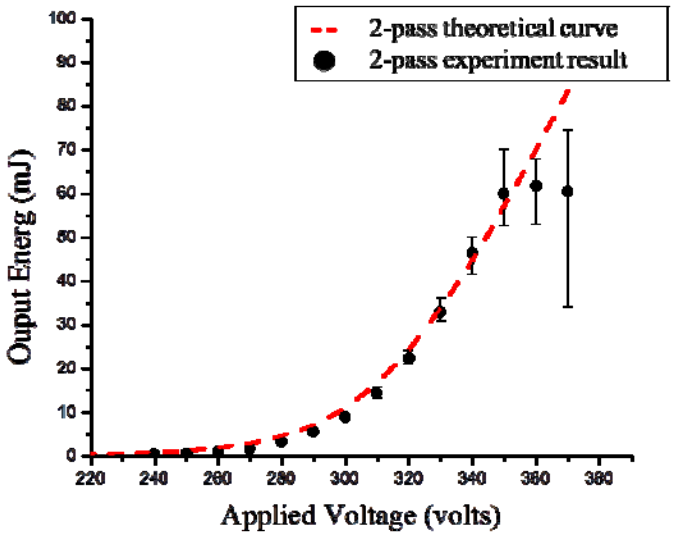

Fig. 3.2.5 The final result of double-pass amplifier. The maximum output energy was 60 mJ.

In Fig. 3.2.5, although ASE occurred much earlier than the previous experiment and limited the maximum output energy to only 360 volts, with an overlap efficiency η_B of 0.46, the output energy (60 mJ) was still higher than which an overlap efficiency η_B is smaller then 0.46. The maximum gain of double-pass amplifier was ~1200 as shown in Fig. 3.2.6.

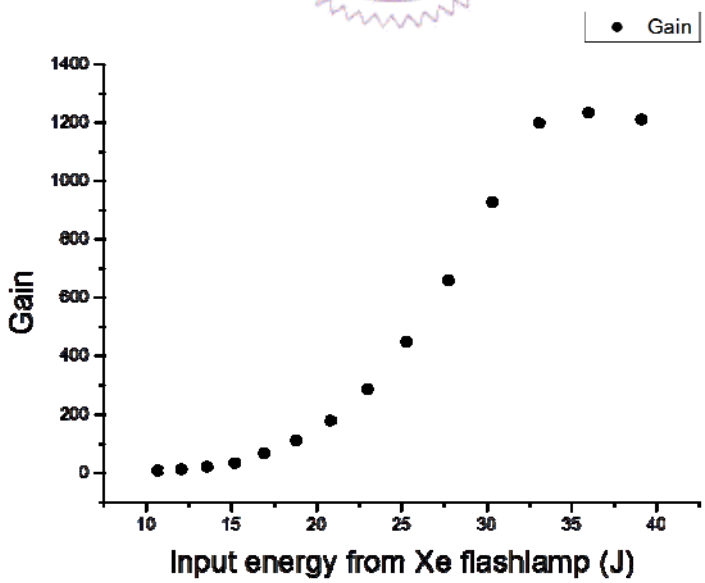

Fig. 3.2.6 The overall energy gain G of double-pass amplifier.

3.3 Second Harmonic Generation

The Non-Critical Phase Matching (NCPM) in LBO crystal can be reached by controlling the temperature along X-axis with a very wide angle acceptance of 52 mrad-cm$^{1/2}$ and no walk-off at all. In our current experiment, the phase-matching temperature was measured at 151^{o}C.

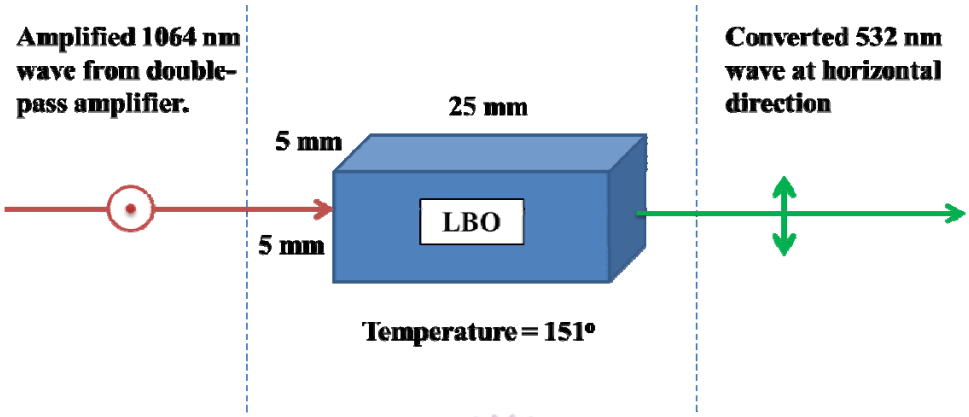

Fig. 3.3.1 Schematic of NCPM type-I SHG.

The experiment setup for SHG is shown in Fig. 3.3.2. The properties of our LBO crystal are 5x5x25 mm^3 with 1064/532nm anti-reflection coating. The damage threshold value for its coating was 1 GW/cm^2 at 1064 nm with 10 ns pulse duration and 10 Hz repetition rate whereas the damage threshold value at 532nm was 0.5 GW/cm^2 under the same conditions. By using the type-I (ooe) second harmonic generation, frequency of the 1064 nm pump wave had been doubled and constitute a wave at 532 nm simultaneously.

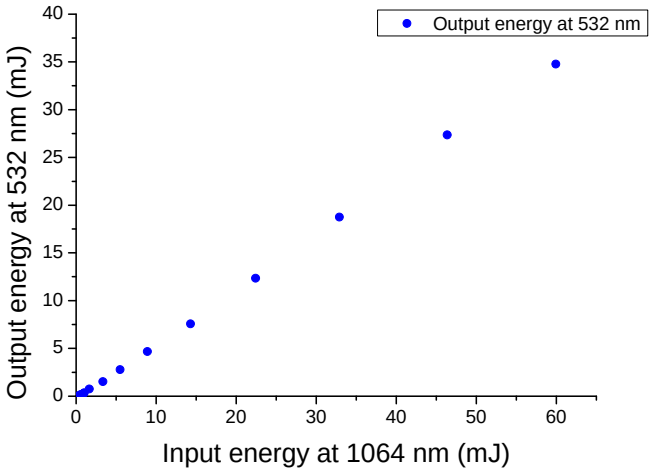

Fig. 3.3.2 Energy converting relation between 1064 nm wave and 532 nm wave. The maximum energy output was 34.7 mJ at 532 nm.

This NCPM type-I SHG fully utilized the effective nonlinearity coefficient $d_{eff} = d_{32}$ at $\phi = 0^o$ and had a better conversion efficiency than angular phase-matching type-I SHG of LBO crystal. In Fig. 3.3.2, the maximum output energy for a 532 nm wave was 35 mJ which was 58% converted from the 1064 nm wave with unfocused input beam of 3.61 mm^2 effective area. The peak intensity of the fundamental wave was calculated as $3.6*10^9$ W/cm^2.

3.4 Laser-induced Wire Radiation

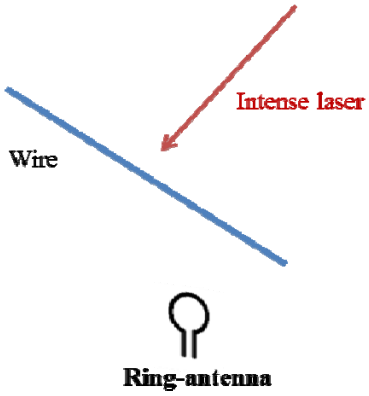

Fig. 3.4.1 Schematic for the laser impacting different wires setup.

At the beginning, we used the amplified fundamental wave at 1064 nm and operated at the maximum output (60 mJ) to impact the different copper wires (60% Cu and 40% Zn) with respect to the diameters of 250 microns and 530 microns. The radiated magnetic field was detected by the ring-antenna detector which is made of a simple wire loop. The results are shown in Fig. 3.4.2a and Fig 3.4.2b:

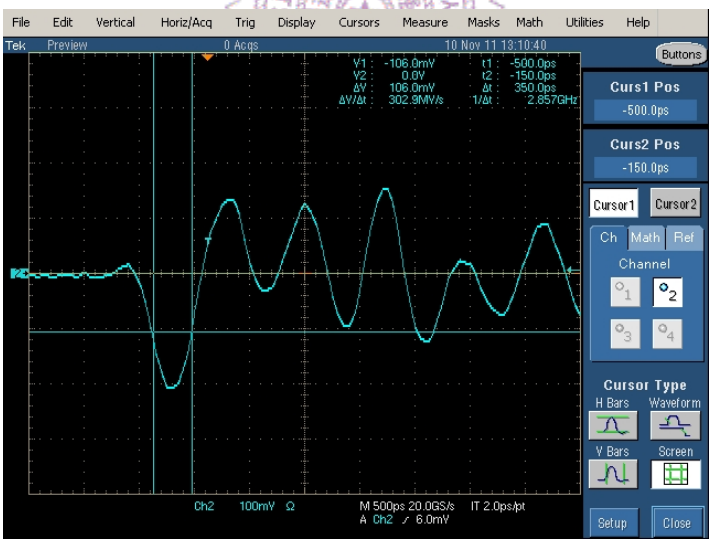

Fig. 3.4.2a The voltage signal is observed on oscilloscope using ring-antenna detector at which the copper diameter is 0.25 mm.

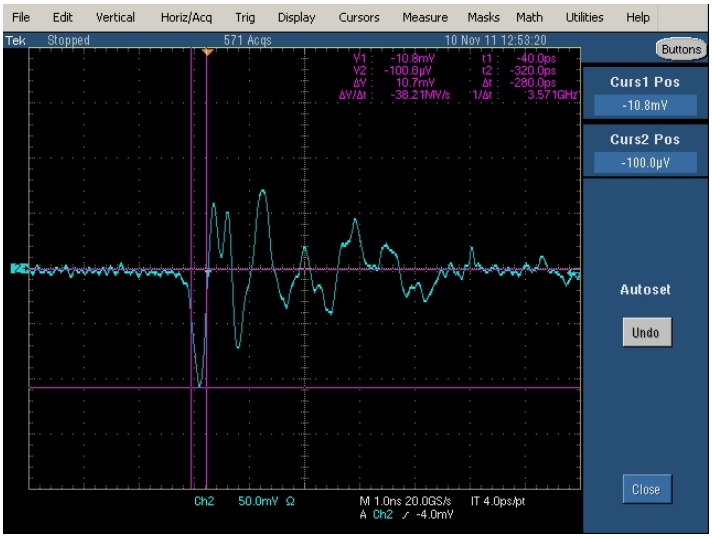

Fig. 3.4.2b The voltage signal is observed on oscilloscope using ring-antenna detector at which the copper diameter is 0.53 mm.

The first peak voltage was 212 mV for the copper wire of 0.25 mm diameter and 100 mV for the one of 0.53 mm diameter. We had also used a thinner copper wire of 0.1 mm diameter and observed a higher voltage than 212 mV but this thin copper wire was cut within few seconds after the laser impacting on its surface.

We further examined the voltage difference between the two ends (one end was grounded) of the wire when the laser was impacting on its surface. A 20 dB attenuator was applied to protect the oscilloscope. Results were shown below:

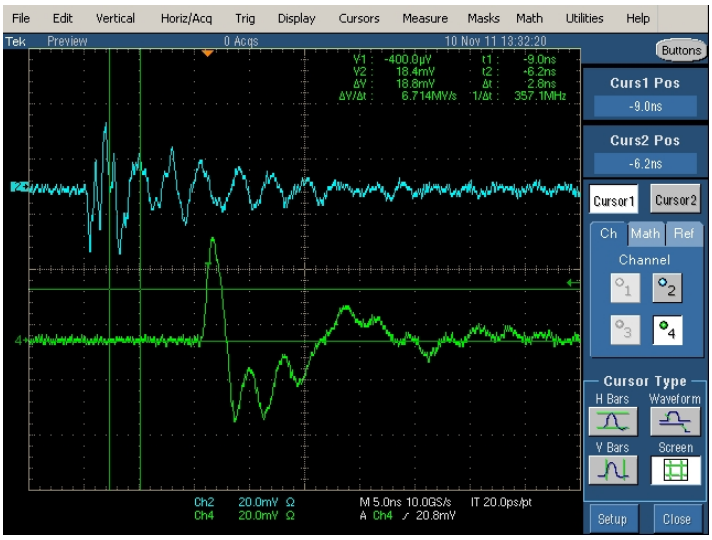

Fig. 3.4.3 The voltage difference (green line) between the two ends of the wire at which the diameter is 0.53 mm. The blue line observed on oscilloscope was detected by using the ring-antenna.

The peak voltage was 37.8 mV which was decayed 100X times through the attenuator. The real voltage should be 3.78 V. Because the oscilloscope had an build-in resistor of 50 ohms, the current in the wire could be calculated as 75.6 mA.

We had used a copper plate as the new target, the setup was shown in Fig. 3.4.4 and the result in Fig. 3.4.5

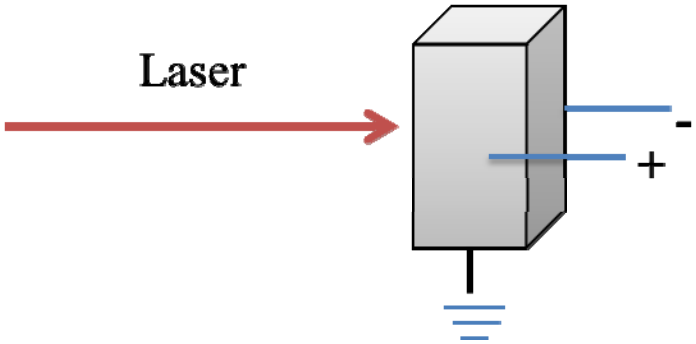

Fig. 3.4.4 The test setup for copper plate.

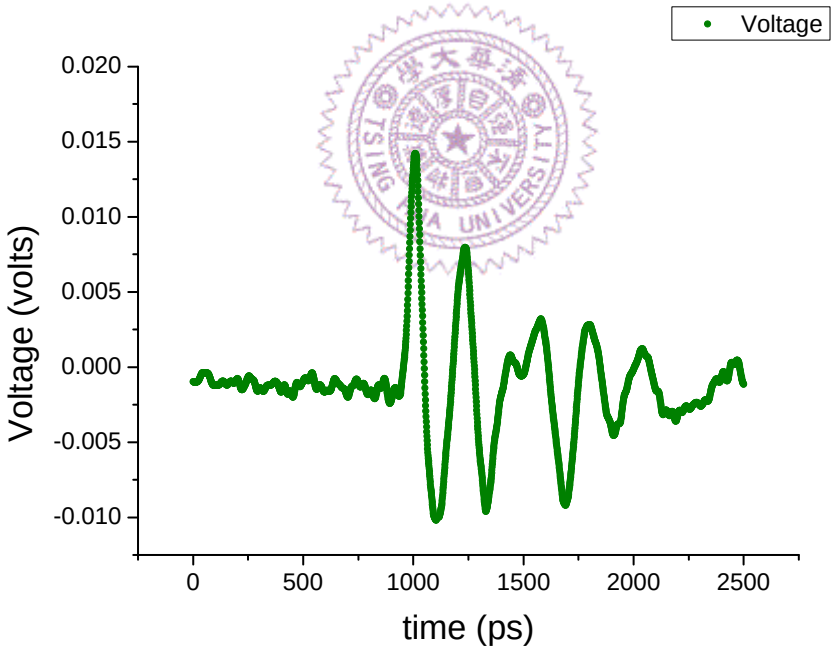

Fig. 3.4.5 The voltage difference (green line) between the two ends of the wire at which the diameter is 0.53 mm. The blue line observed on oscilloscope was detected by using the ring-antenna.

The voltage was 15 mV without any attenuation. Comparing the results between copper wire and copper plate, the induced current was much larger in copper wire.

Then, we coupled the radiation from copper wire (0.53 mm diameter) into a

directional coupler which is the copper rectangular waveguide with a cutoff frequency at 2.078 GHz according to its inner dimension of 34 mm X 72 mm. The setup was shown below:

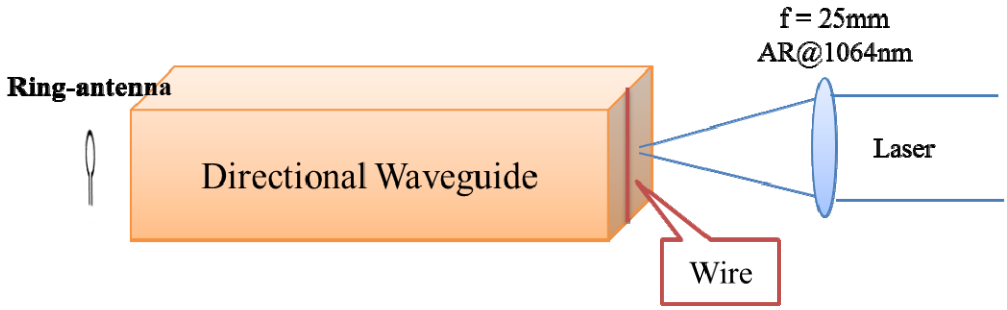

Fig. 3.4.6 Setup for coupling radiation into the directional waveguide at which the signal was generated by linear antenna of the wire. The ring-antenna was put after the direction coupler along vertical direction.

We changed the polarization of the fundamental wave and also put ring-antenna at different positions. The results were shown below:

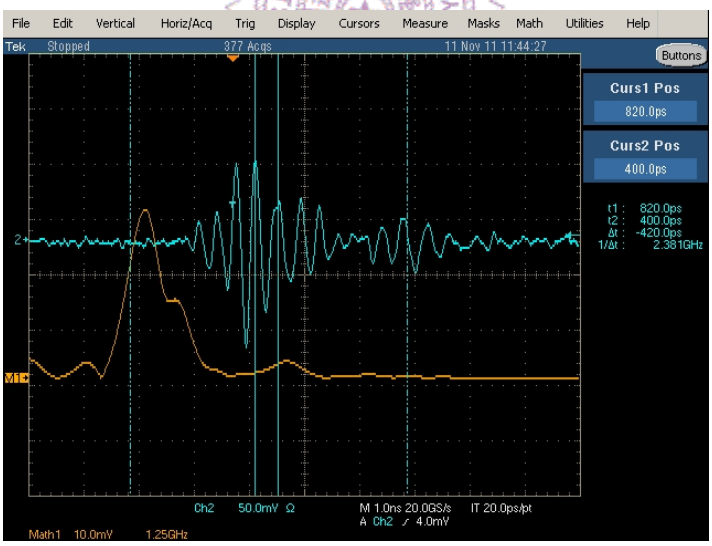

Fig. 3.4.7 The E-field polarized along vertical horizontal and the ring-antenna was put after the directional coupler. The blue curve was the signal detected by the ring-antenna and the orange curve was the FFT result.

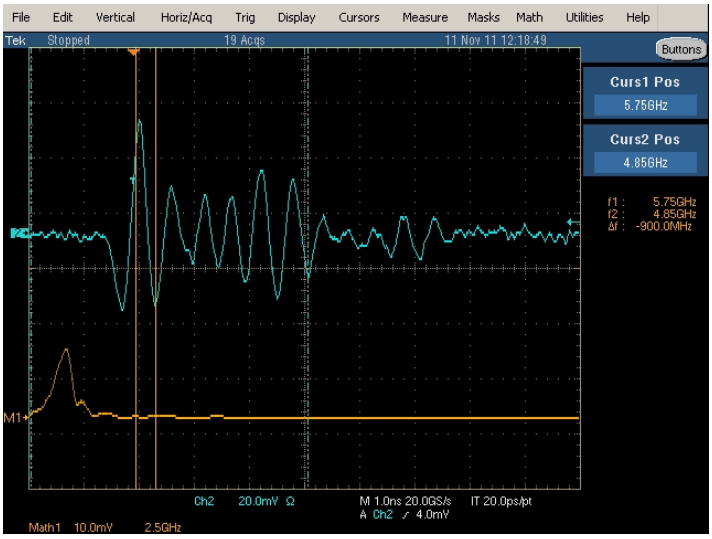

Fig. 3.4.8 The E-field polarized along horizontal direction and the ring-antenna was put in front of the directional coupler. The blue curve was the signal detected by the ring-antenna and the orange curve was the FFT result.

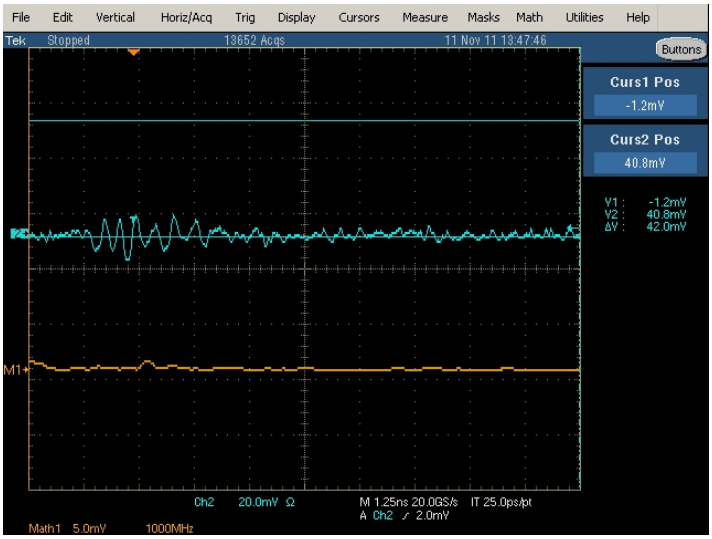

Fig. 3.4.9 The two ends of the wire were insulated from the ground and the ring-antenna was put in front of the directional coupler. The blue curve was the signal detected by the ring-antenna and the orange curve was the FFT result

In Fig. 3.4.7, the central frequency was at 2.62 GHz with the amplitude of 30 mV. The radiation was detected by the ring-antenna, that meat there was a nonzero H_z in the longitudinal direction.

In Fig. 3.4.8, the central frequency was at 1.72 GHz with the amplitude of 12 mV. The lowest cutoff frequency of this directional coupler was 2.078 GHz, therefor, the low frequency radiation would be reflected and received by the ring-antenna

which was put in front of the directional coupler.

In Fig. 3.4.9, the wire was insulated, the electrons from the ground were hard to go into the wire when the electrons were kicked out by the ultra-intense laser. The current flow was very small that made it hard to generate the radiation from dipole antenna.

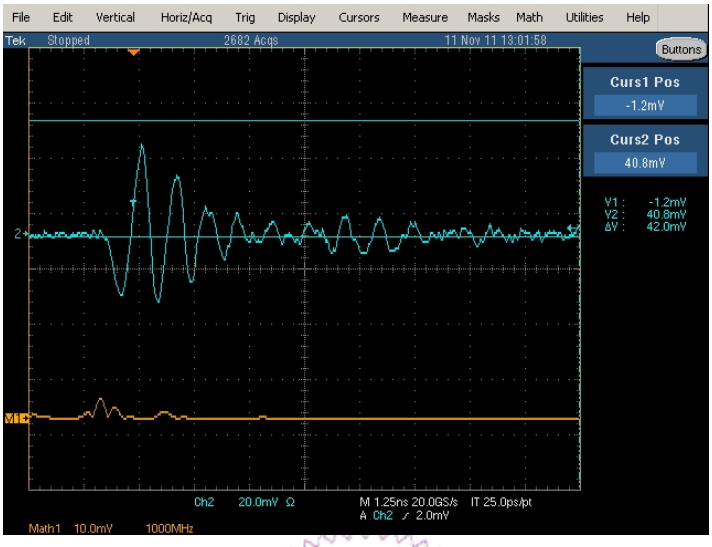

Fig. 3.4.10 The copper wire was placed at the middle along vertical direction and the ring-antenna was put in front of the directional coupler. The blue curve was the signal detected by the ring-antenna and the orange curve was the FFT result

For the setup shown in Fig. 3.4.6, the copper wire was placed at the middle along horizontal direction. Now, we placed the copper wire along vertical direction and we could only observe the radiation in front of the directional coupler by the ring-antenna as shown in Fig. 3.4.10.

Chapter 4 Discussion and Conclusion

4.1 Discussion

There are many commonly used laser amplifiers, Nd^{3+}:YVO_4[13] and Nd^{3+}:YAG are both the commercial laser gain medium for laser amplification at 1064 nm wavelength. Here are some properties for different gain medium listed in Table 4.1.1[14]:

Table 4.1.1 Laser medium properties.

Laser Medium	Transition λ_0 (nm)	Cross Section σ_0 (cm^2)	n
Nd^{3+}:Glass	1053	4E-20	1.5
Nd^{3+}:YAG	1064	3E-19	1.82
Nd^{3+}:YVO_4	1064	8E-19	2.0

The saturation fluence can be calculated as 0.62 J/cm^2 for Nd^{3+}:YAG and 0.23 J/cm^2 for Nd^{3+}:YVO_4, respectively. In chapter 2.1, we said the amplification is exponential only for the input influence is relatively small comparing to the saturation fluence. Our input energy is 50 μJ which indicates the fluence of 0.0017 J/cm^2. Take all the parameters into equation (2.1.20) under our experiment conditions, the energy growth of Nd:YAG medium is faster than Nd:YVO_4 medium as shown in Fig. 4.1.1, that is the reason why we choose Nd:YAG laser rod for our gain medium.

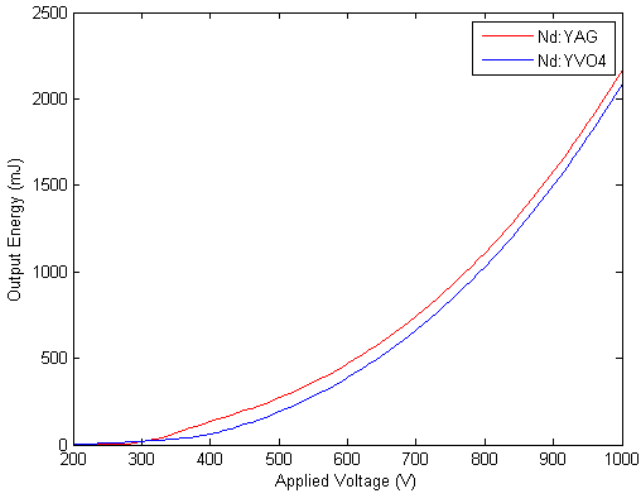

Fig. 4.1.1 Simulation for output energy with different gain medium, Nd:YAG and Nd:YVO_4.

Considering an ideal case for the Nd:YAG amplifier system, with the beam overlap factor equals to 1, the overall energy gain can be more than 4000 at which the output energy can be more than 200 mJ at 360 volts applied voltage. But this is not feasible in the reality as partial reflected wave of a totally overlapped laser which is not fully blocked by the isolator will definitely damage the laser source. As a reason of this, a misalignment of center point has to be achieved in order to direct the reflected beam slightly away from its center.

The conversion efficiency for SHG was 58% which was a typical value for high power pulsed laser. The walk-off angle was almost zero that would be great for another method to generate S-Band radiation by two colors mixing in air plasma if both of the fundamental wave and the second harmonic wave had the intensity higher than 10^{14} W/cm^2 for the ultra-fast laser. At this high intensity, the electrons can be produced by tunneling ionization and then will be forced by the asymmetry electric field to generate electric current inducing radiation [15].

In this experiment, a 2.4GHz-2.6GHz plasma radiation had been elicited by using an ultra-intense laser impacts on the metal wire. After we coupled the wire induced radiation into a direction coupler to filter out the noise of low frequency, a transverse electric (TE) mode with a central frequency of 2.62GHz was found by using a ring-antenna near the copper rectangular waveguide. A simple measure had also been conducted by a half-wave antenna and result showed that, there was a robust signal at its horizontal direction, whereas the vertical signal was trivial. According to these observations, it is believed that the wire excited radiation is operating at a TE_{01} mode, which its field variation has to be further measured in details. In Fig. 3.4.10, when the current flow was along vertical direction in the wire, the thin wire antenna might excite TM mode, but the cutoff frequency of TM_{01} mode was 4.41 GHz which was larger than directional coupler's limitation so that's why we couldn't observe the radiation from the ring-antenna after the directional coupler.

Table 4.1.2 Cutoff frequencies for different modes.

Mode	Cutoff frequency
TE01	2.08 GHz
TE11	4.88 GHz

TE02	4.16 GHz
TM11	4.41 GHz

In Fig. 3.4.8, we did observe low frequency component at 1.7 GHz. Because the spectrum was the FFT result from all components in time domain. The pulse width in each cycle was 100 picoseconds which gave the FWHM of 2.62 ± 2.2 GHz. Therefore, the low frequency component could be produced by the synthesis of multiple cycles.

Furthermore, even though we shifted the original o-wave (in Fig. 3.4.7) to an e-wave by rotating the angle of the half-wave plate (HWP), the wave formation detected by the ring-antenna didn't seems to be altered significantly. This gave us an idea that, the mechanism of radiation emission had no association with the laser's polarization. Instead, when electrons in the wire interacted with an ultra-intense laser, they would absorb the energy from laser to overcome the binding energy that allowed electrons to escape from the metal, the lost electrons would be replaced by pulling electrons from the ground and hence, evokes an electric current.

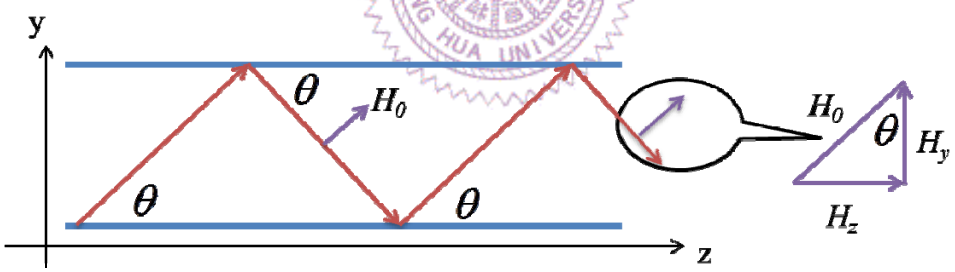

Fig. 4.1.2 The TE_{01} wave propagates in the y-z plane inside the waveguide.

Consider the path of H-field in Fig. 4.1.2, the H_z we measured from ring-antenna was

$$H_z = H_0 \cos(90 - \theta) = H_0 \sqrt{1 - (\frac{\omega_c}{\omega})^2} \qquad (4.1.1)$$

and θ was calculated as 37^o providing H_z=0.6H_0. From equation (B.11) and (2.3.10), the peak current through the wire was calculated as 0.21 ampere and the calculated voltage was 1.056 volts with the load resistor of 50 ohms. Compare the calculated voltage with the result shown in Fig. 3.4.7, the calculated voltage was three times smaller than the measurement result.

In order to improve the conversion efficiency, first, the laser pulse energy must be larger. The mechanism of producing electrons is a multiple ionization process, hence the conversion efficiency will grow nonlinearly with the laser intensity [16]. Second, the wire diameter we used in the experiment was 530 microns, we can use a thinner wire to enhance the radiation power.

4.2 Conclusion

In this paper, we demonstrated an optical pumped S-band radiation generator with 0.021 ampere induced current through the copper wire and 37 watt radiated peak power at 2.62 GHz. The radiation mechanism had weak dependence with laser polarization because the energetic electrons escaped from the copper wire by absorbed the energy provided by the laser to overcome the binding energy.

Based on our current outcomes, further exploration is required to analyze the phenomenon that underlying this radiative mechanism. For examples, different material used in the wire, a variety range of incident angle of the laser and various laser duration pulse…etc., and all of the above parameters are possibly affect the radiation property. Hopefully with the above information, we can further improve and optimize the experiment setup for laser-induced wire radiation.

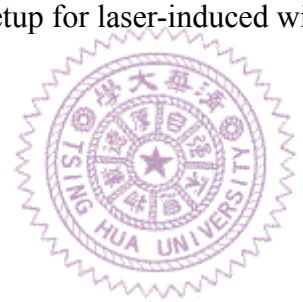

Appendix A

Ring Antenna

A ring-antenna is an inductive loop probe, it is very useful for plasma diagnostic technic for time-varying magnetic fields[12]. The basic principle comes from **Faraday's law** which illustrates a current was induced in a conducting loop when the magnetic flux linking the loop changed. The fundamental relation for electromagnetic induction is

$$\nabla \times \vec{E} = -\frac{\partial \vec{B}}{\partial t} \tag{A.1}$$

where $\vec{E}$ is the electric field vector and $\vec{B}$ is the magnetic flux density field. Taking the surface integral of both sides of equation (A.1) and applying Stokes' theorem, we have

$$\int_S \nabla \times \vec{E} ds = \oint_C \vec{E} dl = -\int_S \frac{\partial \vec{B}}{\partial t} ds \tag{A.2}$$

with a contour C and surface S.

Given a circular loop of N turns wires in the coil and its cross section area A, the equation (A.2) becomes

$$V = -NA\frac{dB}{dt} \tag{A.3}$$

at which the induced voltage is defined as $V = \oint_C \vec{E} dl$.

The design of magnetic field probes is very sensitive to the frequency response desired. The coil dimensions and the time constant are important parameters for the design of the ring-antenna.

Fig. A.1 is an equivalent circuit for the ring-antenna where the L is the self-inductance and Z is the load impedance.

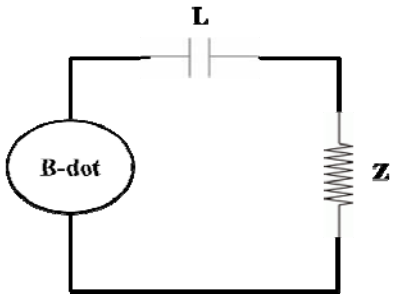

Fig. A.1 Equivalent circuit for the ring-antenna.

When there are N turns wire on the coil with radius r and length l, the self-inductance is

$$L = \frac{r^2 N^2}{9r + 10l} \tag{A.4}$$

and $$\tau = \frac{L}{R}$$ is the time constant (A.5)

When the voltage is induced in the circuit, we have

$$NA\frac{dB}{dt} = L\frac{di}{dt} + iZ$$

$$= \tau\frac{dV_0}{dt} + V_0 \tag{A.6}$$

where i is the circuit current. Solving equation (A.6) with Laplace transforms, we have

$$sB(s)A = si(s)lL + i(s)Z \tag{A.7}$$

and $$i(s) = \frac{sB(s)A}{sL + Z} \tag{A.8}$$

where $s = j\omega$ and $|s| = \omega$.

For high frequency response, most of the voltage in the loop appears across the inductance. At $\omega L >> Z$, we can neglect Z in equation (A.8), leaving

$$i(s) = \frac{B(s)A}{L} \overset{L^{-1}}{\Rightarrow} i(t) = \frac{B(t)A}{L} \tag{A.9}$$

Using $V_0 = iZ$, we have

$$V_0 = \frac{BAZ}{L} = \frac{BA}{\tau} \tag{A.10}$$

For low frequency response, most of the voltage appears across the load impedance. At $\omega L << Z$, we can neglect ωL in equation (A.8), leaving

$$i(s) = \frac{sB(s)A}{Z} \overset{L^{-1}}{\Rightarrow} i(t) = \frac{\dot{B}(t)A}{L} \tag{A.11}$$

Or $$V_0 = \dot{B}(t)A \tag{A.12}$$

Appendix B

Rectangular Waveguide

Consider a rectangular waveguide in Fig. B.1, with its cross section of sides ***a*** and ***b***. The enclosed conductor is assumed to have constitutive parameters ε and μ. We will discuss the properties of three EM waves (TM, TE and TEM) propagating in the waveguide[10].

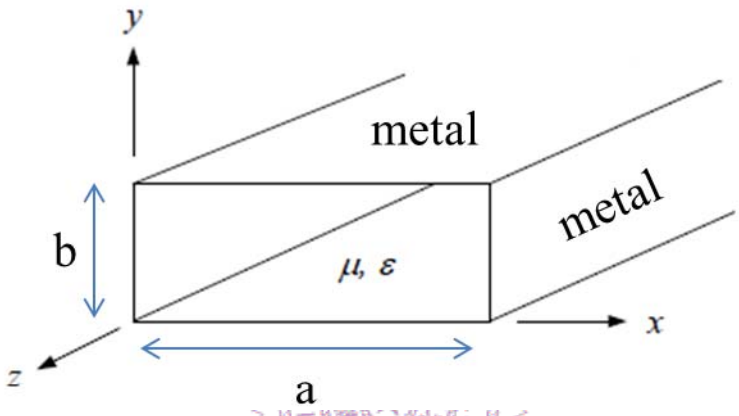

Fig. B.1 Schematic for a rectangular metal waveguide.

Proceeding from the Maxwell curl equations:

$$\nabla \times \overline{E} = \begin{vmatrix} \hat{x} & \hat{y} & \hat{z} \\ \frac{\partial}{\partial x} & \frac{\partial}{\partial y} & \frac{\partial}{\partial z} \\ E_x & E_y & E_z \end{vmatrix} = -j\omega\mu\overline{H}$$

and

$$\nabla \times \overline{H} = \begin{vmatrix} \hat{x} & \hat{y} & \hat{z} \\ \frac{\partial}{\partial x} & \frac{\partial}{\partial y} & \frac{\partial}{\partial z} \\ E_x & E_y & E_z \end{vmatrix} = j\omega\varepsilon\overline{E}$$

We have the following equations:

$\nabla \times \overline{E} = -j\omega\mu\overline{H}$		$\nabla \times \overline{H} = j\omega\varepsilon\overline{E}$	
$\frac{\partial H_z}{\partial y} + \beta H_y = j\omega\varepsilon E_x$	(B.1)	$\frac{\partial E_z}{\partial y} + \beta E_y = -j\omega\mu H_x$	(B.4)
$-\frac{\partial H_z}{\partial x} - \beta H_x = j\omega\varepsilon E_y$	(B.2)	$-\frac{\partial E_z}{\partial x} - \beta E_x = -j\omega\mu H_y$	(B.5)

$\frac{\partial H_y}{\partial x} - \frac{\partial H_x}{\partial y} = j\omega\varepsilon E_z$ (B.3)	$\frac{\partial E_y}{\partial x} - \frac{\partial E_x}{\partial y} = -j\omega\mu H_z$ (B.6)

By manipulating these equations we can express the transverse fields in terms of the two longitudinal components E_z and H_z. We have

$$H_x = \frac{j}{k_c^2}\left(\omega\varepsilon\frac{\partial E_z}{\partial y} - \beta\frac{\partial H_z}{\partial x}\right) \quad \text{(B.7)}$$

$$H_y = \frac{-j}{k_c^2}\left(\omega\varepsilon\frac{\partial E_z}{\partial x} - \beta\frac{\partial H_z}{\partial y}\right) \quad \text{(B.8)}$$

$$E_x = \frac{-j}{k_c^2}\left(\beta\frac{\partial E_z}{\partial x} + \omega\varepsilon\frac{\partial H_z}{\partial y}\right) \quad \text{(B.9)}$$

$$E_y = \frac{j}{k_c^2}\left(-\beta\frac{\partial E_z}{\partial y} + \omega\varepsilon\frac{\partial H_z}{\partial x}\right) \quad \text{(B.10)}$$

With the boundary conditions in rectangular metal waveguide, we can solve the equations by the method of separation of variables. The details will not discuss here, we only list the results in Table.

Table B.1 Properties of rectangular metal waveguide for TE_{mn} and TM_{mn} modes.

	TE_{mn} mode	TM_{mn} mode
k_c	$\sqrt{\left(\frac{m\pi}{a}\right)^2 + \left(\frac{n\pi}{b}\right)^2}$	$\sqrt{\left(\frac{m\pi}{a}\right)^2 + \left(\frac{n\pi}{b}\right)^2}$
f_c	$\frac{1}{2\sqrt{\mu\varepsilon}}\sqrt{\left(\frac{m}{a}\right)^2 + \left(\frac{n}{b}\right)^2}$	$\frac{1}{2\sqrt{\mu\varepsilon}}\sqrt{\left(\frac{m}{a}\right)^2 + \left(\frac{n}{b}\right)^2}$
E_z	0	$B_{mn}\sin\frac{m\pi}{a}x\sin\frac{n\pi}{b}ye^{-j\beta z}$
H_z	$A_{mn}\cos\frac{m\pi}{a}x\cos\frac{n\pi}{b}ye^{-j\beta z}$	0
E_x	$\frac{j\omega\mu n\pi}{k_c^2 b}A_{mn}\cos\frac{m\pi}{a}x\sin\frac{n\pi}{b}ye^{-j\beta z}$	$\frac{-j\beta m\pi}{k_c^2 a}B_{mn}\cos\frac{m\pi}{a}x\sin\frac{n\pi}{b}ye^{-j\beta z}$
E_y	$\frac{-j\omega\mu m\pi}{k_c^2 a}A_{mn}\sin\frac{m\pi}{a}x\cos\frac{n\pi}{b}ye^{-j\beta z}$	$\frac{-j\beta n\pi}{k_c^2 b}B_{mn}\sin\frac{m\pi}{a}x\cos\frac{n\pi}{b}ye^{-j\beta z}$
H_x	$\frac{j\beta m\pi}{k_c^2 a}A_{mn}\sin\frac{m\pi}{a}x\cos\frac{n\pi}{b}ye^{-j\beta z}$	$\frac{j\omega\varepsilon n\pi}{k_c^2 b}B_{mn}\sin\frac{m\pi}{a}x\cos\frac{n\pi}{b}ye^{-j\beta z}$
H_y	$\frac{j\beta n\pi}{k_c^2 b}A_{mn}\cos\frac{m\pi}{a}x\sin\frac{n\pi}{b}ye^{-j\beta z}$	$\frac{-j\omega\varepsilon m\pi}{k_c^2 a}B_{mn}\cos\frac{m\pi}{a}x\sin\frac{n\pi}{b}ye^{-j\beta z}$

For TM modes in rectangular metal waveguide, neither ***m*** nor ***n*** can be zero. Hence, the TM_{11} mode is the dominant mode which has the lowest cutoff frequency of all TM modes.

For TE modes, either ***m*** or ***n*** can be zero but not both of them. If a>b, the TE_{10} is the dominant mode or if b>a, then the TE_{01} mode is the dominant mode.

For the TEM wave, it is characterized as $E_z=0$ and $H_z=0$. From equation (B.7)~(B.10), it can be shown that all the transverse fields are zero. This means there is no TEM mode in the rectangular metal waveguide.

The time-average power flowing through a cross section of the waveguide for TE_{10} mode is calculated as

$$P(z) = \int_0^b \int_0^a -\frac{1}{2}(E_y)(H_x)^* dxdy = \omega\mu\beta ab(a\frac{H_0}{2\pi})^2 \tag{B.11}$$

The power will lose after propagating a distance in the waveguide if there are losses in the dielectric and in the imperfectly conducting guide walls. The attenuation constant due to loss in the dielectric is given by

$$\alpha_d = \frac{\sigma\eta}{2\sqrt{1-(f_c/f)^2}} \tag{B.12}$$

The attenuation constant due to loss in the guide walls is defined as

$$\alpha_c = \frac{P_L(z)}{2P(z)} \tag{B.13}$$

where $P_L(z)$ is the time-average power lost in the guide walls. For TE_{10} mode, α_c is calculated as

$$\alpha_c = \frac{1}{\eta b}\sqrt{\frac{\pi f\mu_c}{\sigma_c\left[1-(f_c/f)^2\right]}}\left[1+\frac{2b}{a}(\frac{f_c}{f})^2\right] \tag{B.14}$$

where σ_c is the conductivity of the conductor and is the permeability μ_c of the conductor.

Reference

[1] Hamster H., Sullivan A., Gordon S., White W. and Falcone R.W. "Subpicosecond electromagnetic pulses from intense laser-plasma interaction". Phys. Rev. Lett. 71, 2725 (1993).

[2] Kress M., Loffler T., Susanne E., Mark T., and Roskos H. G. " Terahertz-pulse generation by photoionization of air with laser pulses composed of both fundamental and second-harmonic waves". Optics Letters. Vol. 29, Issue 10, pp. 1120-1122 (2004).

[3] Kreb, M. et al. "Determination of the carrier-envelope phase of few-cycle laser pulses with terahertzemission spectroscopy". Nature Phys. 2, 327–331 (2006)

[4] Andrey S., Yong Y., Young C. and Alexander F. "Non-equilibrium plasma in liquid water: dynamics of generation and quenching". Plasma Sources Sci. Technol. 20 024003.

[5] Hache´, A. et al. "Observation of coherently controlled photocurrent in unbiased, bulk GaAs". Phys. Rev. Lett. 78, 306–309 (1997).

[6] AjayNahata, N., Weling, A. S. and Heinz, T. F. "A wideband coherent terahertz spectroscopy system using optical rectification and electro-optic sampling", Appl. Phys. Lett. **69**, 2321 (1996).

[7] Fitzgerald, A. J., Berry, E., Zinovev, N. N., Walker, G. C., Smith, M. A. and Chamberlain, J. M. "An introduction to medical imaging with coherent terahertz frequency radiation", Phys. Med. Biol. 47 R67 (2002).

[8] Koechner, W., "Solid state laser engineering", Springer, 6th, (2006).

[9] Huang, Y. C. "Nonlinear Optics", (2003).

[10] Li Z. C. and Jian Z. "Terahertz radiation from a wire target irradiated by an ultra-intense laser pulse", PHYSICS OF PLASMAS, 14, 054505 (2007).

[11] Cheng D. K. "Field and wave electromagnetics", second edition.

[12] Kirtley D. E. "Study of the Synchronous Operation of an Annular Field Reversed Conguration Plasma Device", PHD thesis, University of Michigan (2008).

[13] Brignon A., Feugnet G., Huifnard J. -P. and Pocholle J. -P., " Compact Nd:YAG and Nd: YVO_4 Amplifiers End-Pumped by a High-Brightness Stacked Array", IEEE Journal of Quantum Electronics, Vol. 34, No. 3, (1998).

[14] Saleh B. E. A., Teich M. C., "Fundamentals of Photonics", Wiley, 2nd, (2007).

[15] Kim1 K. Y., Taylor1 A. J., Glownia1 J. H. and Rodriguez1 G., "Coherent control of terahertz supercontinuum generation in ultrafast laser–gas

interactions “, Nature Photonics 2, 605 - 609 (2008).
[16] Mainfray G., and Manus G., “Multiphoton Ionization of Atoms”, Rep. Prog. Phys. 54 1333, (1991)